

## Effective mass of high-mobility $\text{In}_2\text{O}_3$ -based transparent conductive oxides fabricated by solid-phase crystallization

Takashi Koida<sup>1,\*</sup> and Junichi Nomoto<sup>2</sup>

<sup>1</sup>Research Institute for Energy Conservation, National Institute of Advanced Industrial Science and Technology (AIST), 1-1-1, Umezono, Tsukuba, 305-8568, Japan

<sup>2</sup>Advanced Manufacturing Research Institute, National Institute of Advanced Industrial Science and Technology (AIST), 1-1-1, Higashi, Tsukuba, 305-8565, Japan



(Received 7 February 2022; accepted 18 April 2022; published 11 May 2022)

Polycrystalline  $\text{In}_2\text{O}_3$  films, which are solid-phase crystallized (spc) from amorphous films doped with hydrogen (H) and transition metals (TMs), exhibit remarkably high mobilities ( $100\text{--}160\text{ cm}^2\text{ V}^{-1}\text{ s}^{-1}$ ); moreover, their specific resistance is equivalent to  $2\text{--}3 \times 10^{-4}\ \Omega\text{ cm}$  or less, even when the carrier density is reduced to one-fifth ( $1\text{--}4 \times 10^{20}\text{ cm}^{-3}$ ) that of conventional transparent conductive oxide (TCO) films. The high mobility and low carrier density significantly reduce free-carrier absorption, and the transparent region of the TCO films extends across the visible and near-infrared regions. In this study, we experimentally demonstrate that *spc*- $\text{In}_2\text{O}_3\text{:H}$  and  $\text{In}_2\text{O}_3\text{:TM,H}$  films with an impurity concentration of less than a few at. % exhibit superior mobility compared to that of optimized  $\text{In}_2\text{O}_3\text{:Sn,H}$  films ( $\sim 70\text{ cm}^2\text{ V}^{-1}\text{ s}^{-1}$ ) with similar Sn and close-carrier concentrations. Photoelectron spectroscopy measurements revealed that the electronic state of the *spc* films, including the valence of TM impurities, changed with varying In/O ratios of the amorphous films. Furthermore, the In, O, TM, and H compositions in the amorphous films were found to be critical for effective activation of  $\text{TM}_{\text{In}}^+$ ,  $\text{H}_{\text{O}}^+$ , and  $\text{H}_i^+$  donors after crystallization. To determine the origin of the high electron mobility, the effective mass and relaxation time of electrons in these films were evaluated by spectroscopic ellipsometry. The results showed that the high mobility could be primarily attributed to the long relaxation time instead of the small effective mass. Additionally, the dispersion of conduction bands near the Fermi energy was found to be almost independent of the type of metallic impurity (Sn, H, Ce, Zr, and W) for the investigated impurity concentrations. Moreover, the increase in relaxation time by H and TM doping was examined.

DOI: [10.1103/PhysRevMaterials.6.055401](https://doi.org/10.1103/PhysRevMaterials.6.055401)

### I. INTRODUCTION

Transparent conductive oxide (TCO) with high electron mobility ( $>100\text{ cm}^2\text{ V}^{-1}\text{ s}^{-1}$ ) exhibit higher conductivity, lower absorption coefficients, and extended transparency compared to those of conventional TCO [1–3].  $\text{In}_2\text{O}_3$  with  $\sim 1$  at. % transition metal (TM; Ti, Zr, Hf, Mo, W, and Ce) and/or hydrogen (H) impurities shows a significantly higher mobility than that of Sn-doped  $\text{In}_2\text{O}_3$  ( $\text{In}_2\text{O}_3\text{:Sn}$ , ITO), which is widely used as a TCO film with decent transparency in the visible region [2–4]. In particular, polycrystalline  $\text{In}_2\text{O}_3$  films, which are solid-phase crystallized (spc) from amorphous films doped with H or both H and TM, exhibit considerable mobility ( $\sim 160\text{ cm}^2\text{ V}^{-1}\text{ s}^{-1}$ ), and the specific resistance can be equivalent to  $2\text{--}3 \times 10^{-4}\ \Omega\text{ cm}$  or less, even if the carrier density is reduced to one-fifth that of conventional ITO films [4]. Consequently, these films exhibit high transparency even in the near-infrared region without compromising their high conductivity. These films can be formed on various underlying layers and substrates by low-temperature ( $150\text{--}200\text{ }^\circ\text{C}$ ) processes. Therefore, incorporation of TCO films in window electrodes could improve the performance of existing optoelectronic de-

vices and enable development of new optoelectronic devices with sensitivity in both the visible and near-infrared ( $800\text{--}1700\text{ nm}$ ) regions, such as ultraefficient multijunction solar cells and surface-irradiated near-infrared image sensors.

The report on *spc*- $\text{In}_2\text{O}_3\text{:H}$  [5] has attracted attention in the photovoltaic industry because it can directly facilitate improvements in conversion efficiency by reducing optical loss [6] and reduce the cell price by decreasing the amount of In used [7]; this can be achieved by replacing the conventional ITO with a high-mobility thin TCO film as the window electrode in Si heterojunction solar cells, which show the highest conversion efficiency among Si solar cells. Consequently, research has been actively conducted on solar cells [8–14] incorporating the  $\text{In}_2\text{O}_3\text{:H}$ -based TCOs and their practical applications to include this material in existing manufacturing processes. The following strategies have been attempted for integrating this material into current manufacturing frameworks: (1) development of methods to introduce H into TCO films, such as adding a small amount of water vapor [5] as a hydrogen source to the equipment of physical vapor deposition methods, such as magnetron sputtering (MS) and reactive plasma deposition (RPD); use of Ar gas with a controlled dew point [15]; introduction of hydrogen and oxygen gases [11,16] instead of water vapor; and use of residual gas in the equipment without intentionally introducing the hydrogen

\*t.koida@aist.go.jp

source gases, based on the fact that the residual gas in a deposition chamber contains degas components of water adsorbed on the inner wall and sample tray of the chamber [4,12]; (2) determination of TMs to be added along with H [4,14,17–19], and production of raw-material tablets for RPD and high-density conductive sputtering targets that can be stably used in production lines; and (3) manufacturing microstructured TCO films with reliable long-term electrical properties [20]. Consequently, certain cell manufacturers have recently employed high-mobility TCO layers in the window electrodes of Si heterojunction solar cells using a new RPD tablet or an MS target instead of ITO. Additionally, applications for other solar cells [21–26] and near-infrared sensors [27] have been reported at the R&D level.

The theoretical understanding of these materials is also being advanced. First-principles calculations using density-functional theory (DFT) initially suggested that H could function as a donor in high electron-affinity oxide semiconductors [28–30]. After the experimental discovery of H-doped  $\text{In}_2\text{O}_3$  as a degenerate wide-gap semiconductor with high mobility [5],  $\text{H}_\text{O}^+$  with  $\text{H}^-$  substitution was theoretically clarified to act as a donor in addition to  $\text{H}_\text{i}^+$  in the oxygen antibonding site in the degenerate state in which the Fermi energy is higher than that of the conduction-band minimum (CBM) [31]. Calculations of the adsorption, dissociation, and reaction of  $\text{H}_2\text{O}$  and  $\text{H}_2$  molecules on the  $\text{In}_2\text{O}_3$  surface have provided important insight into H and OH uptake on the growing surface of thin films when  $\text{H}_2\text{O}$  or  $\text{H}_2$  is used as the hydrogen source [32,33]. Although the dominant defect species and their states in  $\text{In}_2\text{O}_3$  containing both H and TM have not yet been clarified, several calculations for TM-containing  $\text{In}_2\text{O}_3$  have been reported [34–38]. Recently, Xu *et al.* systematically investigated the doping behavior of TMs (3d, 4d, and 5d in groups 4–6) or Sn, a group 14 element, in terms of the TM *d*-orbital or Sn 5s-orbital energy levels referenced to the CBM of  $\text{In}_2\text{O}_3$  [38]. In the case of Sn doping, Sn 5s orbitals strongly mix with In 5s orbitals, altering the band dispersion near the CBM and increasing the effective mass of electrons. Because mobility can be expressed as electron charge  $\times$  relaxation time/effective mass, an increase in the effective mass decreases the mobility. In contrast, the modest interactions between the *d* orbitals of TMs and the In 5s orbitals do not significantly alter the band dispersion near the CBM; therefore, the increase in effective mass is not observed as in ITO. Moreover, the *d*-orbital levels of Zr, Hf, and Ta are located in the conduction band of  $\text{In}_2\text{O}_3$  at energies considerably higher than the CBM. These TMs can be ionized and electronically doped into the conduction band, and their Fermi energies are sufficiently lower than the empty *d*-orbital levels, permitting high-concentration doping. A similar effect can be expected for the Ce doping analyzed in the present study because the Ce 4*f* orbitals do not similarly interact with the In 5s orbitals [37]. Furthermore, the defect states and their concentrations have been calculated when the Fermi energy, chemical potential of O (oxygen partial pressure), and temperature were varied [38]. Therefore, computational science has provided results that typically require significant effort and time to be acquired experimentally, and the calculation-based energy-level scheme can be further improved by considering the hybridization from the O 2*p* orbitals around the dopant and

the ligand field of the octahedral coordination [39]. Consequently, the appropriate impurity elements for achieving high mobility can be theoretically determined in the future.

However, experimental reports on the effective mass of electrons in high-mobility TCO films are limited [36,40–42]. The ITO film typically used as a comparison material is a common ITO film (5, 10 wt. %  $\text{SnO}_2$ ) with a considerably higher Sn concentration than that of the TMs. Therefore, most of the reported effective masses of ITO correspond to ITO films with carrier densities as high as  $\sim 1 \times 10^{21} \text{ cm}^{-3}$ . Therefore, the possible existence of noteworthy differences in electron mobility and effective mass compared to those of optimized low-Sn concentration ITO films has not yet been clarified.

In this study, the possible superior mobility of H/TM impurity-containing  $\text{In}_2\text{O}_3$  thin films, which were solid-phase crystallized after unheated film deposition, compared to that of the low Sn-concentration ITO was experimentally clarified. During film deposition, an In/O ratio suitable for the metal impurities and their added amounts were carefully determined. Specifically, several film materials were prepared by varying the oxygen flow ratio during film deposition and systematically modifying the In/O ratio in amorphous (*a*-) films. During solid-phase crystallization, a nitrogen atmosphere was used to prevent the supply of oxygen or hydrogen to the films. The actual changes in the In/O ratio of the thin films were confirmed by thermal desorption spectroscopy (TDS). Photoelectron spectroscopy was employed to evaluate the electronic states of In, O, and the metal impurities at the core level and near the valence-band maximum (VBM). The effective mass and relaxation time of electrons in these films were calculated by spectroscopic ellipsometry (SE) to determine the factor responsible for the high mobility. Radio-frequency MS and RPD were employed to deposit the thin films.  $\text{In}_2\text{O}_3\text{:H}$ ,  $\text{In}_2\text{O}_3\text{:Me,H}$  (Me: Sn, Ce, Zr), and  $\text{In}_2\text{O}_3\text{:Ga,Ti,Zr,H}$  were prepared by MS, and  $\text{In}_2\text{O}_3\text{:H}$  and  $\text{In}_2\text{O}_3\text{:Me,H}$  (Me: Sn, Ce, W) were prepared by RPD.

## II. EXPERIMENT

Approximately 60-nm-thick  $\text{In}_2\text{O}_3$  films were deposited on  $\text{SiO}_2/\text{Si}$  substrates by radio-frequency MS (Eiko Engineering) [43] and in-line RPD (Sumitomo Heavy Industries, URT-IP2) [44], and subsequently characterized. The RPD instrument is an ion-plating system for thin-film deposition that uses a pressure-gradient type plasma gun. Compared to MS, RPD has a lower energy of deposited particles and a higher ionization rate [45]. The following ceramic targets and tablets with different impurities were used: (1) pure  $\text{In}_2\text{O}_3$ ;  $\text{In}_2\text{O}_3$  containing 0.5, 1, and 2 wt. %  $\text{CeO}_2$ ;  $\text{In}_2\text{O}_3$  containing 1 wt. %  $\text{ZrO}_2$ ;  $\text{In}_2\text{O}_3$  containing 1, 2, and 5 wt. %  $\text{SnO}_2$ ; and a commercially available TM-containing  $\text{In}_2\text{O}_3$  containing less than 1 wt. % each of  $\text{ZrO}_2$ ,  $\text{TiO}_2$ , and  $\text{Ga}_2\text{O}_3$  targets for MS; (2) pure  $\text{In}_2\text{O}_3$ ;  $\text{In}_2\text{O}_3$  containing 1 wt. %  $\text{WO}_3$ ;  $\text{In}_2\text{O}_3$  containing 1, 2, and 3 wt. %  $\text{CeO}_2$ ; and  $\text{In}_2\text{O}_3$  containing 1, 3, and 5 wt. %  $\text{SnO}_2$  tablets for RPD. Ar,  $\text{O}_2$ , and  $\text{H}_2\text{O}$  were used as deposition gases at a total pressure of  $\sim 0.4$  Pa in both methods. The flow ratio of  $\text{O}_2$  to Ar +  $\text{O}_2$  [ $F(\text{O}_2)$ ] was varied (0–1% for MS and 8–24% for RPD). The water vapor partial pressure ( $P_{\text{H}_2\text{O}}$ ) was fixed at  $1 \times 10^{-4}$  Pa for MS and varied from  $1 \times 10^{-5}$

to  $5 \times 10^{-4}$  Pa for RPD prior to monitoring the deposition by quadrupole mass spectrometry (Inficon, Transpector XPR3). All the films were deposited without intentional substrate heating, and the maximum substrate temperatures were observed using thermolabels attached to the  $\text{SiO}_2/\text{Si}$  substrates ( $<50^\circ\text{C}$  for MS and  $60^\circ\text{C}$  for RPD). All of the *spc* films were prepared by postannealing the corresponding *a* films at  $250^\circ\text{C}$  for 30 min in a  $\text{N}_2$  atmosphere with heating and cooling rates of  $20^\circ\text{C}/\text{min}$ . The H contents of the initial *a* films were 1.5–4.0 at. %,  $\sim 10\%$  of which is known to effuse during crystallization [4,5]. Films were also deposited as H-free films by MS without intentionally introducing water vapor. The base pressure of the MS system was less than  $3 \times 10^{-6}$  Pa. The TM:In atomic ratio of the thin films deposited by sputtering without substrate heating was expected to be similar to that of the ceramic targets; however, the atomic ratio in the RPD samples varied with the vapor pressure of the raw material. In the *a*- $\text{In}_2\text{O}_3$ :W,H ( $\text{WO}_3$ : 1 wt. %) and  $\text{In}_2\text{O}_3$ :Ce,H (CeO<sub>2</sub>: 1, 2, 3 wt. %) films prepared at an  $F_{\text{RPD}}(\text{O}_2)$  of 24%, the TM (W, Ce):In atomic ratios were measured by inductively coupled plasma mass spectrometry (ICP-MS) to be 0.95, 0.28, 0.96, and 1.3 at. %, respectively [4]. A W:In ratio of 0.39 was previously determined by our group for the same film [4]; however, ICP-MS measurements with a different etching solvent yielded a ratio of 0.95, which reflected the actual atomic ratio in the thin film. The structural properties of the *spc* films fabricated by RPD have been reported elsewhere [4], and those of the films fabricated by MS were similar to previously reported values [5,41]. The electrical properties were determined using a Hall measurement system (Toyo, ResiTest8300). Desorption gases from the films during heating in a vacuum were monitored by TDS (Esco, EMD-1000S) using 220-nm-thick films on  $\text{SiO}_2/\text{Si}$ .  $\text{O}_2$  [molecular-mass/charge ( $m/z$ ) = 32] and In ( $m/z$  = 115) were also measured. *a* films were characterized instead of *spc* films because the signals from the *a* films included information on the desorption gasses during both solid-phase crystallization and high-temperature annealing of the crystallized films. Thick films were used only in this context to improve the signal-to-noise ratio. Electronic states of the films were evaluated by synchrotron hard-x-ray photoelectron spectroscopy (HAXPES) using the BL46XU beamline at SPring-8 (photon energy:  $h\nu = 7.939$  keV). The optical effective mass and relaxation time were evaluated using SE spectra, which were acquired from ultraviolet to infrared wavelengths using two rotating-compensator ellipsometry systems [200–1700 nm (J. A. Woolam, M-2000) and 1.7–30  $\mu\text{m}$  (J. A. Woolam, IR-VASE)]. The SE analyses of the films were performed using an optical model consisting of air/surface roughness layer/TCO/ $\text{SiO}_2$ /crystalline Si [see inset of Fig. 7(b)]. To simplify the SE analysis, thickness and optical constants of  $\text{SiO}_2$  film were taken from the measurement of the  $\text{SiO}_2/\text{Si}$  substrate prior to deposition. The dielectric function of the  $\text{In}_2\text{O}_3$ :Me,H layer was modeled by combining the Drude model with the Tauc-Lorentz (TL) model. The SE data allow us to obtain surface roughness, thickness, and optical constants of the  $\text{In}_2\text{O}_3$ :Me,H films. From the analyses of the dielectric function, high-frequency dielectric constant, effective mass ( $m^*$ ), and optical mobility ( $\mu_{\text{opt}}$ ) can be obtained. Here,  $m^*$  values are calculated assuming that the optical carrier density ( $N_{\text{opt}}$ ) is the same as electrically active carrier

density obtained by Hall measurements. Details regarding the measurement and data analysis procedures in the ultraviolet to infrared regions can be found elsewhere [41].

### III. RESULTS AND DISCUSSION

#### A. Synthesis of *spc*- $\text{In}_2\text{O}_3$ :Me,H films with controlled oxygen stoichiometry

Controlling  $P_{\text{H}_2\text{O}}$  during unheated film deposition is crucial for fabricating *spc*- $\text{In}_2\text{O}_3$ :Me,H films [5,15]. The effects of water vapor on structural and electrical properties are clearly illustrated in Fig. 1. The films prepared without intentional introduction of water vapor had a polycrystalline structure with grain sizes of 20–50 nm containing several lattice defects in the as-deposited state [Fig. 1(a-1)]; the crystallinity did not change even after postannealing [(Fig. 1(b-1)]. The electrical properties of these films were degraded, except for the ITO containing 2 or 5 wt. %  $\text{SnO}_2$  [Figs. 1(a-2) and 1(b-2)]. The carrier density decreased, and the mobility was significantly degraded in the films fabricated at high  $F_{\text{MS}}(\text{O}_2)$  probably owing to the reduced effective activation of the metal dopant due to a certain fraction of the dopant atoms not occupying the In lattice sites in  $\text{In}_2\text{O}_3$ . The significantly lower standard formation enthalpies per mole of metal of CeO<sub>2</sub> and ZrO<sub>2</sub> compared to those of  $\text{SnO}_2$  and  $\text{In}_2\text{O}_3$  ( $-1088.7$ ,  $-1100.6$ ,  $-577.6$ , and  $-462.9$  kJ mol<sup>-1</sup>, respectively) corroborate this result [46]. Additionally, the scattering at charged grain boundaries significantly contributes to the mobility of polycrystalline films, especially at low carrier densities [47]. Consequently, the specific resistance varies by orders of magnitude depending on the type of the Me and  $F_{\text{MS}}(\text{O}_2)$ . In contrast, the samples prepared by introducing water vapor showed mostly amorphous although it contained some crystalline structures in the as-deposited state [Fig. 1(c-1)]. The mobility gradually degraded with increasing metal-impurity concentration [Fig. 1(c-2)]. Upon postannealing, these films were solid-phase crystallized, and polycrystalline films with high crystallinity were formed [Fig. 1(d-1)], whose resistivity was less than  $1 \times 10^{-3}$   $\Omega$  cm [Fig. 1(d-2)]. The individual grains were submicrometer-sized single-crystalline-like grains [41], and the Me and H impurities could be considered to be solidly soluble as metastable supersaturated solid solutions at the given postannealing temperature [20]. The grain sizes are much larger than the mean-free path of free electrons expected from the measured carrier density and mobility [48]. In addition, as described in Sec. III C, the Hall mobility in the *spc* films is comparable to optical mobility, suggesting that the potential barrier for free electrons formed at the grain boundaries is negligible, as previously examined [20,41]. These factors are responsible for the lower resistivity than those of the polycrystalline films fabricated without water vapor [Fig. 1(b-2)]. Consequently, the Hall mobility in the *spc* films is governed by scattering within the grains, and the effects of the Me and hydrogen impurities and the defects derived from the In/O ratio on mobility can be examined.

Controlling  $F_{\text{MS}}(\text{O}_2)$  under the controlled  $P_{\text{H}_2\text{O}}$  during unheated film deposition is also important for fabricating *spc* films with high electron mobility. For example, in

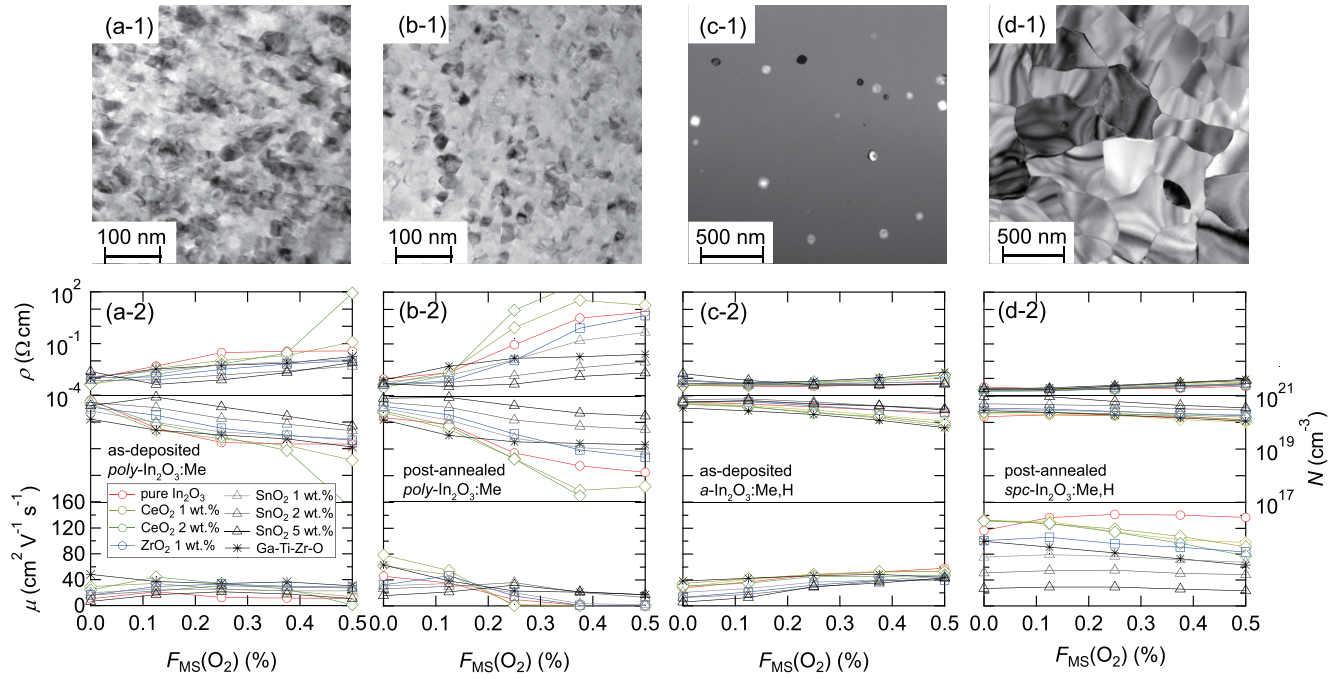


FIG. 1. (1) Plan-view TEM images and (2) electrical properties [resistivity ( $\rho$ ), carrier density ( $N$ ), and mobility ( $\mu$ )] of (a) as-deposited and (b) postannealed polycrystalline  $\text{In}_2\text{O}_3:\text{Me}$  films deposited without intentionally adding water vapor, and (c) as-deposited amorphous and (d) postannealed solid-phase crystallized  $\text{In}_2\text{O}_3:\text{Me,H}$  films deposited under an optimized water-vapor pressure. In (1), TEM images for metallic-impurity free  $\text{In}_2\text{O}_3$  are shown.

metallic-impurity-free  $\text{In}_2\text{O}_3$ , both carrier density and mobility increased with the introduction of  $\text{O}_2$  from the  $\text{O}_2$ -free state, and the highest mobility was achieved at an optimal  $F_{\text{MS}}(\text{O}_2)$  of  $\sim 0.5\%$  [Fig. 2(a)]. Further increase in  $F_{\text{MS}}(\text{O}_2)$  reduces both carrier density and mobility. Figure 2(b) shows variation of carrier density and mobility during heating from room temperature to  $200^\circ\text{C}$  and during cooling from  $200$  to  $40^\circ\text{C}$  in vacuum. During the heating over  $150^\circ\text{C}$ , all the films show strong decrease in carrier density and increase in mobility. This behavior is attributed to the change in carrier generation and scattering mechanisms. After crystallization,

mobility increases with decreasing temperature for all the *spc* films, and the slope for the film deposited at the optimal  $F_{\text{MS}}(\text{O}_2)$  is the largest among the films. The results suggest that impurity scattering is significantly suppressed, and phonon scattering appears to prevail in the film. The impurity defects can be ascribed to stoichiometry deviation in the *spc* films. Figure 2(c) shows spectra for gases desorbed from the *a* films during high-temperature annealing in a vacuum. The desorption of In was detected at  $160^\circ\text{C}$  during crystallization and at  $420^\circ\text{C}$  for the thin films prepared under less-than-optimal  $F_{\text{MS}}(\text{O}_2)$  conditions, whereas the desorption of  $\text{O}_2$

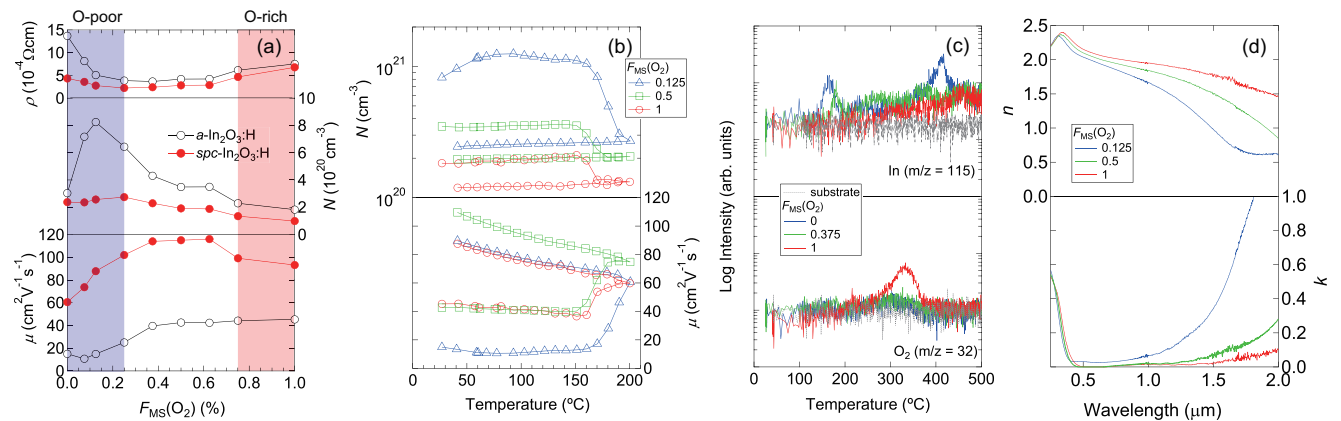


FIG. 2. (a) Resistivity ( $\rho$ ), carrier density ( $N$ ), and mobility ( $\mu$ ) values of *a*- and *spc*- $\text{In}_2\text{O}_3:\text{H}$  films as a function of oxygen flow ratio [ $F_{\text{MS}}(\text{O}_2)$ ] during magnetron sputtering (MS). (b)  $N$  and  $\mu$  of  $\text{In}_2\text{O}_3:\text{H}$  films deposited at different  $F_{\text{MS}}(\text{O}_2)$  values as a function of temperature. The properties were measured during heating from room temperature to  $200^\circ\text{C}$  and during cooling from  $200$  to  $40^\circ\text{C}$  in vacuum. During the heating, solid-phase crystallization occurred at temperatures over  $150^\circ\text{C}$ . (c) TDS profiles of substrate and *a*- $\text{In}_2\text{O}_3:\text{H}$  films for In (115) and  $\text{O}_2$  (32). (d) Refractive index ( $n$ ) and extinction coefficient ( $k$ ) of *spc*- $\text{In}_2\text{O}_3:\text{H}$  films obtained by point-by-point fitting.

was detected at 330 °C for the films prepared under  $F_{\text{MS}}(\text{O}_2)$  values higher than the optimum. These observations clearly suggest the existence of excess elements or vacancies in the *spc* films prepared at 250 °C, which acted as scattering centers owing to the deviation from the optimal In/O ratio, decreasing the mobility of the films [Figs. 2(a) and 2(b)]. According to first-principles DFT calculations, oxygen vacancies ( $V_{\text{O}}$ ) are more likely to be formed in  $\text{In}_2\text{O}_3$  than interstitial In ( $\text{In}_i$ ) under O-poor conditions, whereas interstitial oxygen ( $\text{O}_i$ ) is more likely to be formed than In vacancies ( $V_{\text{In}}$ ) under O-rich conditions [49]. The fabricated thin films were solid-phase crystallized by postannealing of unheated thin films prepared using a nonequilibrium process. For films with an  $F_{\text{MS}}(\text{O}_2)$  close to zero, the absorption in the visible region was significantly higher [Fig. 2(d)], suggesting the formation of oxygen vacancies with a mixture of indium metal clustered with  $\text{In}_i$ . Evidently, in *spc*- $\text{In}_2\text{O}_3$ :H thin films prepared by direct current MS using an  $\text{In}_2\text{O}_3$  ceramic target under an  $\text{O}_2$ -gas-free Ar atmosphere, the In metal in the films was clearly observed by transmission electron microscope-energy dispersive x-ray spectroscopy [50]. On the other hand, *spc* films fabricated above the optimal  $F_{\text{MS}}(\text{O}_2)$  are transparent in the visible region, suggesting the absence of  $\text{In}_i$ . Moreover, the transparency extends to the near-infrared region owing to low free-carrier absorption. Based on the results, the  $F_{\text{MS}}(\text{O}_2)$  value of 0 in the present study corresponds to a chemical potential close to that of the oxygen formed by In. Therefore, the variation in  $F_{\text{MS}}(\text{O}_2)$  in this study corresponds to a gradual increase in the chemical potential of oxygen from the extreme O-poor condition. As the  $F_{\text{MS}}(\text{O}_2)$  decreases from the optimum ( $\sim 0.5$ ) to 0,  $V_{\text{O}}$  increases and, in certain cases,  $\text{In}_i$  even forms clustered In metal; moreover, as the  $F_{\text{MS}}(\text{O}_2)$  increases from the optimum ( $\sim 0.5$ ) to 1, the  $\text{O}_i$  concentration increases.

The optimal  $F_{\text{MS}}(\text{O}_2)$  for enabling high mobility depended on the impurity and its added amount. In Fig. 1(d-2), the optimal  $F_{\text{MS}}(\text{O}_2)$  corresponding to maximum mobility decreased with the amount of Ce doping, and the maximum mobility was observed when the films were prepared using Ar only for the *spc*- $\text{In}_2\text{O}_3$ :Ce,H (CeO<sub>2</sub>: 1, 2 wt %) films; no such absorption was found in the visible region for *spc*- $\text{In}_2\text{O}_3$ :H. At an  $F_{\text{MS}}(\text{O}_2)$  of 0.5%, the carrier density hardly varied with increasing Ce content, and the mobility rapidly decreased. Considering that the targets were prepared by mixing and sintering  $\text{In}_2\text{O}_3$  and CeO<sub>2</sub> powders, the mixed targets can be expressed as  $\text{In}_{2-2x}\text{Ce}_{2x}\text{O}_{3+x}$ , in which the oxygen composition is higher than that in the  $\text{In}_2\text{O}_3$  target. Therefore, even for identical  $F_{\text{MS}}(\text{O}_2)$  values, the chemical potential of oxygen on the growing surface of the thin films was higher than that of  $\text{In}_2\text{O}_3$ . Moreover, as the  $F_{\text{MS}}(\text{O}_2)$  increased, the amount of O incorporated into the film per Ce atom increased from 1.5 to 2 to maintain charge neutrality, leading to a decrease in the In/O ratio of the *a* film. When the films were postannealed and crystallized, the  $V_{\text{O}}$  concentration decreased, and the mobility increased in the films prepared under low- $F_{\text{MS}}(\text{O}_2)$  conditions compared to that of the Ce-free films. In contrast, the excess oxygen in the thin films prepared under high- $F_{\text{MS}}(\text{O}_2)$  conditions induced the formation of  $\text{O}_i$ , which compensated the free carriers and decreased the mobility. The actual valence of Ce in the thin film is discussed in the HAXPES analysis. In this experiment, the process window of the optimal  $F_{\text{MS}}(\text{O}_2)$  for a

high-Ce content film was extremely narrow, with an  $F_{\text{MS}}(\text{O}_2)$  close to zero; however, the process window could be widened by applying a reduced target, using direct-current MS instead of radio-frequency MS, or introducing H<sub>2</sub> gas instead of H<sub>2</sub>O. In the RPD method used in this study, which is also effective, an  $\text{In}_2\text{O}_3$  ceramic tablet sublimates as  $\text{In}_2\text{O}$  upon heating, which is ionized by plasma and deposited on the substrate. The optimal  $F_{\text{RPD}}(\text{O}_2)$  determined by RPD, which showed similar optoelectrical properties to those of *a*- $\text{In}_2\text{O}_3$ :H and *spc*- $\text{In}_2\text{O}_3$ :H prepared by MS, was  $\sim 24\%$ ; this value is considerably higher than that of MS ( $\sim 0.5\%$ ). Therefore, the optimal  $F_{\text{RPD}}(\text{O}_2)$  for  $\text{In}_2\text{O}_3$ :Ce,H films can be readily achieved by RPD, and thin films with a lower chemical potential of oxygen than that of the Ar-only thin films prepared by MS can be fabricated at a low  $F_{\text{RPD}}(\text{O}_2)$ .

### B. Electronic states of *spc*- $\text{In}_2\text{O}_3$ :Me,H films

This section analyzes changes in the electronic states of the thin films, including the valence of TM impurities, with varying In/O ratios. Figure 3 shows the valence band (VB), near VBM, and core-level spectra of Ce (Ce  $2p_{3/2}$ ) or W (W  $3d_{5/2}$ ) for as-deposited amorphous and solid-phase crystallized  $\text{In}_2\text{O}_3$ :Ce,H and  $\text{In}_2\text{O}_3$ :W,H films prepared by RPD at  $F_{\text{RPD}}(\text{O}_2)$  values of 15 and 24%. The core-level spectra of In (In  $3d_{5/2}$ ) and O (O  $1s$ ) for these films are shown in the Supplemental Material (Fig. S1) [51]. Here, the VB signal intensities are normalized by their integrated areas to compare the amorphous and crystalline thin films, and the VBM spectra are an enlarged version of the VB spectra. Moreover, the core-level signals are normalized by the signal peak intensity. The tail states at the VBM and the lower edge of the VB at  $\sim 9$  eV decreased after crystallization [Figs. 3(a-1) and 3(b-1)] [52,53]. The magnitude of the CBM emission was reduced with an increase in the low  $F_{\text{RPD}}(\text{O}_2)$  in the amorphous thin films and when the films were crystallized [Figs. 3(a-2) and 3(b-2)]; the magnitudes correspond to the carrier densities listed in Table I. In the *a*- $\text{In}_2\text{O}_3$ :Me,H films [ $F_{\text{RPD}}(\text{O}_2) = 15\%$ ] prepared by RPD, a large density of states was observed from the VBM to binding energy ( $E_{\text{b}}$ ) of 1.4 eV, which can be attributed to the presence of partially unsaturated In cations and/or large void defects originating from oxygen deficiencies [54–56]. The core-level spectra of In and O were asymmetric (Fig. S1 in the Supplemental Material [51]) owing to the free-electron–core-hole coupling in the conduction band [57,58]. Specifically, photoelectrons can access two different final states: the unscreened state (high- $E_{\text{b}}$  side), wherein the state localized below the Fermi level is empty, and the screened state (low- $E_{\text{b}}$  side), wherein it is filled by electrons from the conduction band. The probability of screening should increase with increasing carrier density. Evidently, the asymmetry was greater for the films with high carrier densities. An OH-derived peak was also observed at the high binding-energy side of the O core level (Fig. S1 in the Supplemental Material [51]).

The core-level behavior of Ce is worth focusing on. Figure 3(a-3) shows the Ce  $2p_{3/2}$  spectra, which contain mixed states of Ce<sup>3+</sup> and Ce<sup>4+</sup>. During fitting, the relative positions and intensity ratios of peaks corresponding to the Ce<sup>4+</sup> and Ce<sup>3+</sup> states (green and blue curves, respectively) were

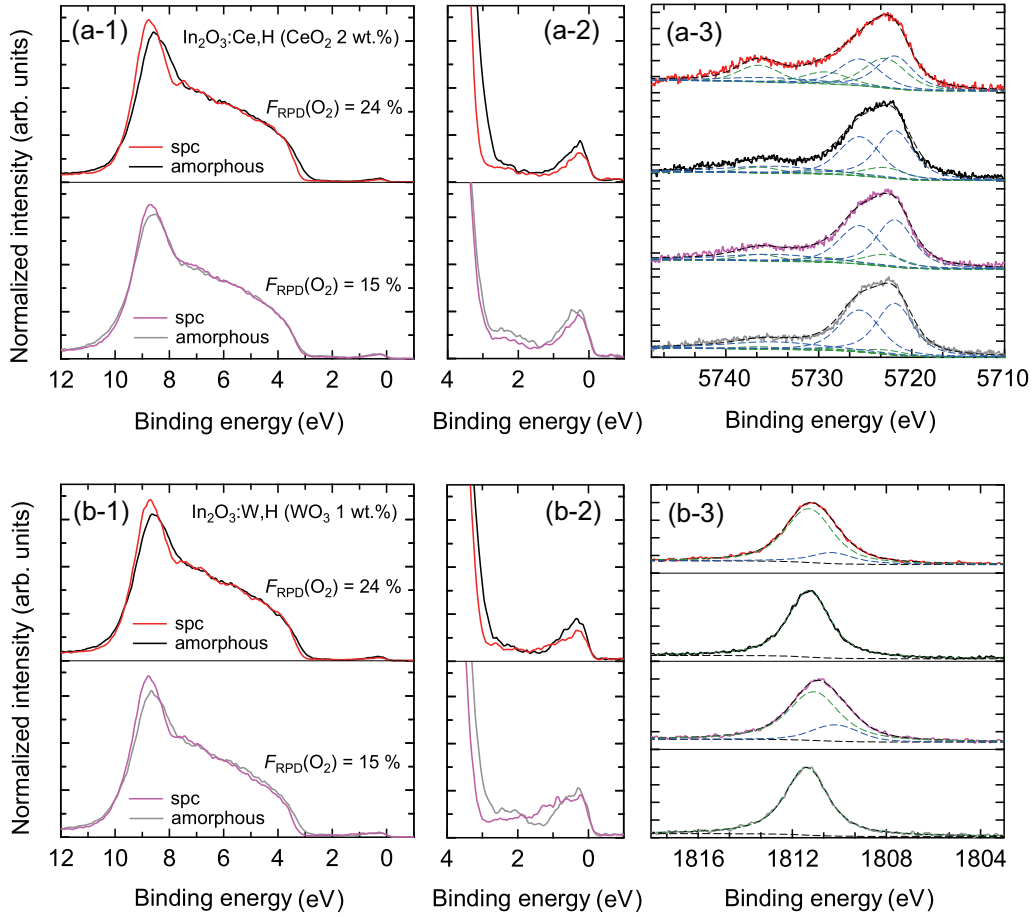


FIG. 3. Spectra near the (1) valence band, (2) valence-band minimum, and (3) Ce  $2p_{3/2}$  or W  $3d_{5/2}$  core-level spectra of as-deposited amorphous and solid-phase crystallized (a)  $\text{In}_2\text{O}_3:\text{Ce,H}$  and (b)  $\text{In}_2\text{O}_3:\text{W,H}$  films prepared by RPD at different  $F_{\text{RPD}}(\text{O}_2)$  values.

TABLE I. Properties of  $\text{In}_2\text{O}_3:\text{TM,H}$  films (TM: Ce, W): ceramic tablet or target material, structure [amorphous ( $a$ -) or solid-phase crystallized ( $spc$ -)],  $F_{\text{RPD}}(\text{O}_2)$  and  $F_{\text{MS}}(\text{O}_2)$ , resistivity ( $\rho$ ), carrier density ( $N$ ), Hall mobility ( $\mu$ ), percentages of  $\text{Ce}^{3+}$  and  $\text{Ce}^{4+}$  ( $C_{\text{III}}\%$ ,  $C_{\text{IV}}\%$ ), and percentages of  $\text{W}^{4+}$  and  $\text{W}^{6+}$  ( $C_{\text{IV}}\%$ ,  $C_{\text{VI}}\%$ ).

Material	Structure	$F(\text{O}_2)$		Electrical properties			Valence-state ratio	
		$F_{\text{RPD}}(\text{O}_2)$ (%)	$F_{\text{MS}}(\text{O}_2)$ (%)	$\rho$ ( $\Omega \text{ cm}$ )	$N$ ( $\text{cm}^{-3}$ )	$\mu$ ( $\text{cm}^2 \text{ V}^{-1} \text{ s}^{-1}$ )	( $\text{Ce}^{3+}$ , $\text{Ce}^{4+}$ )	( $\text{W}^{4+}$ , $\text{W}^{6+}$ )
$\text{In}_2\text{O}_3:\text{Ce,H}$ (2 wt. % $\text{CeO}_2$ )	$a$ -	15		$4.5 \times 10^{-4}$	$4.5 \times 10^{20}$	31	(92, 8)	
	$spc$ -	15		$2.7 \times 10^{-4}$	$2.8 \times 10^{20}$	84	(78, 22)	
	$a$ -	24		$5.7 \times 10^{-4}$	$2.3 \times 10^{20}$	47	(81, 19)	
	$spc$ -	24		$2.2 \times 10^{-4}$	$1.8 \times 10^{20}$	157	(50, 50)	
$\text{In}_2\text{O}_3:\text{Ce,H}$ (3 wt. % $\text{CeO}_2$ )	$spc$ -	24		$4.8 \times 10^{-4}$	$1.7 \times 10^{20}$	78	(49, 51)	
$\text{In}_2\text{O}_3:\text{Ce,H}$ (1 wt. % $\text{CeO}_2$ )	$spc$ -		0	$2.0 \times 10^{-4}$	$2.4 \times 10^{20}$	133	(38, 62)	
	$spc$ -		0.5	$5.7 \times 10^{-4}$	$1.2 \times 10^{20}$	91	(17, 83)	
$\text{In}_2\text{O}_3:\text{Ce,H}$ (2 wt. % $\text{CeO}_2$ )	$spc$ -		0	$2.0 \times 10^{-4}$	$2.4 \times 10^{20}$	131	(59, 41)	
	$spc$ -		0.5	$5.1 \times 10^{-4}$	$1.6 \times 10^{20}$	78	(39, 61)	
$\text{In}_2\text{O}_3:\text{W,H}$ (1 wt. % $\text{WO}_3$ )	$a$ -	15		$3.9 \times 10^{-4}$	$5.4 \times 10^{20}$	30		(0, 100)
	$spc$ -	15		$1.8 \times 10^{-4}$	$3.6 \times 10^{20}$	96		(21, 79)
	$a$ -	24		$4.5 \times 10^{-4}$	$3.0 \times 10^{20}$	47		(0, 100)
	$spc$ -	24		$5.3 \times 10^{-4}$	$1.5 \times 10^{20}$	81		(17, 83)

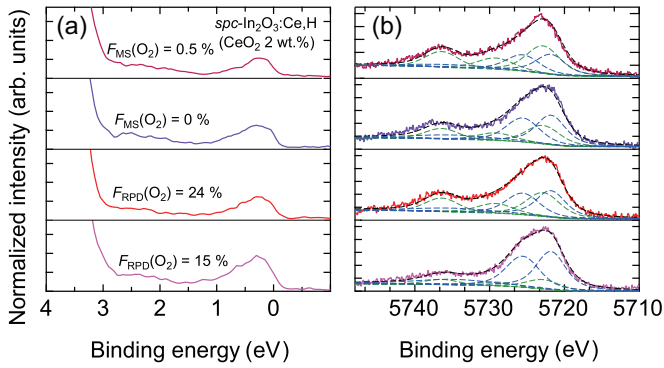


FIG. 4. (a) Spectra near the VBM and (b) core-level spectra of Ce  $2p_{3/2}$  for  $spc\text{-In}_2\text{O}_3\text{:Ce,H}$  films prepared by RPD and MS with varying  $F_{\text{RPD}}(\text{O}_2)$  and  $F_{\text{MS}}(\text{O}_2)$ , respectively.

fixed using previously reported values for three prominent components, which were attributed to the three final state configurations for  $\text{Ce}^{4+}$  ( $2p^54f^2$ ,  $2p^54f^1$ , and  $2p^54f^0$ ), and two prominent components, which were attributed to the two final-state configurations for  $\text{Ce}^{3+}$  ( $2p^54f^2$  and  $2p^54f^1$ ) [59]. Table I summarizes the percentages of  $\text{Ce}^{3+}$  and  $\text{Ce}^{4+}$  ( $C_{\text{III}}\%$ ,  $C_{\text{IV}}\%$ ) in the  $\text{In}_2\text{O}_3\text{:Ce,H}$  films; those in the amorphous films prepared at  $F_{\text{RPD}}(\text{O}_2)$  values of 15 and 24% were (92, 8) and (81, 19), respectively. When these films were solid-phase crystallized, the percentages changed to (78, 22) and (50, 50), respectively. The increased ratio of  $\text{Ce}^{4+}$  in the amorphous films can be ascribed to the increased amount of O incorporated into the films owing to the increase in oxygen partial pressure during deposition. Moreover, the increased ratio of  $\text{Ce}^{4+}$  by crystallization can be explained by the reduction in elastic energy around the Ce atoms substituted in the In sites. Owing to the ionic radii of the six-coordinated  $\text{In}^{3+}$ ,  $\text{Ce}^{3+}$ , and  $\text{Ce}^{4+}$  (80, 101, and 87 pm, respectively) [60], a large structural distortion presumably occurred upon substitution of the trivalent Ce in the In site. If the valence of the Ce is changed to  $4+$ , the elastic energy can be reduced. Carrier generation due to the change in valence is discussed later. Reinterpreting the obtained results from this perspective,  $\text{Ce}^{3+}$  was found to be stably present, especially in the  $spc\text{-In}_2\text{O}_3\text{:Ce,H}$  film prepared at a low  $F_{\text{RPD}}(\text{O}_2)$ . In this film, abundant oxygen vacancies or defects in which hydrogen, with its small ionic radius, is substituted for oxygen sites likely exist. Therefore, even if the large ionic-radius  $\text{Ce}^{3+}$  is substituted into the In site, structural relaxation due to the presence of  $V_{\text{O}}$  or  $\text{H}_{\text{O}}$  occurs, leading to an insignificant increase in the total elastic energy. Therefore, the structure is presumed to be maintained with a large proportion of  $\text{Ce}^{3+}$  even after crystallization. This reasoning also explains the behavior of the  $\text{In}_2\text{O}_3\text{:Ce,H}$  films prepared by MS. The 0%  $F_{\text{MS}}(\text{O}_2)$  for  $spc\text{-In}_2\text{O}_3\text{:Ce,H}$  ( $\text{CeO}_2$ : 1 and 2 wt. %) was an optimal or a slightly O-rich condition, as described earlier. Therefore, a higher  $\text{Ce}^{4+}$  ratio was achieved by MS than that by RPD. The  $\text{Ce}^{4+}$  ratio further increased with increasing  $F_{\text{MS}}(\text{O}_2)$  (Fig. 4 and Table I).

The origin of the free carriers is analyzed herein. The carrier density systematically increased with Ce concentration in the optimized films prepared by RPD and MS [see Figs. 1(d) and 6]. However, the increase in  $\text{Ce}^{4+}$  did not escalate the carrier density in the films with similar amounts of Ce doping

[Table I and Figs. 4(a) and 4(b)]. In contrast, the increase in  $\text{Ce}^{3+}$  amplified the carrier density. This indicates the existence of a donor impurity other than  $\text{Ce}^{4+}$ , which can be explained by the contribution of H ( $\text{H}_i^+$  and  $\text{H}_\text{O}^+$ ) as a donor, as observed in  $spc\text{-In}_2\text{O}_3\text{:H}$  [5,41]. The presence of the H donor and/or  $\text{O}_i$  compensating for the carriers strongly affects the carrier density of the films. If the In/O ratio of an amorphous film is more than  $2/3$  owing to In-rich deposition conditions, and the valence of Ce changes from  $3+$  to  $4+$  by crystallization, Ce functions as a monovalent ionization donor ( $\text{Ce}_{\text{In}}^+$ ) in the crystallized film. H functions as an  $\text{H}_i^+$  and  $\text{H}_\text{O}^+$  donor. Moreover, when the In/O ratio is less than  $2/3$  owing to O-rich deposition conditions, carrier compensation can occur in the form of  $\text{O}_i$  in the vicinity of  $\text{Ce}^{4+}$ , unless excess O is released from the film as  $\text{O}_2$  or  $\text{H}_2\text{O}$ . Under these conditions, H has an extremely low concentration of  $\text{H}_\text{O}^+$ , and functions exclusively as an  $\text{H}_i^+$  donor. This indicates that adjusting the compositions of In, O, Ce, and H in the thin film is critical for effective activation of the  $\text{Ce}_{\text{In}}^+$ ,  $\text{H}_\text{O}^+$ , and  $\text{H}_i^+$  donors. In fact, an increased carrier density by Ce addition and a higher carrier density than that in poly- $\text{In}_2\text{O}_3\text{:Ce}$  without H deposited on heated substrates were achieved in our previous study by adjusting  $F_{\text{RPD}}(\text{O}_2)$ ,  $P_{\text{H}_2\text{O}}$ , and temperature during film deposition [4].

A change in the valence of W was also observed in the W-containing films [Fig. 3(b-3)]. Table I also summarizes the percentages of  $\text{W}^{4+}$  (blue curve) and  $\text{W}^{6+}$  (green curve) ( $C_{\text{IV}}\%$ ,  $C_{\text{VI}}\%$ ) in the  $\text{In}_2\text{O}_3\text{:W,H}$  films. Only the hexavalent species was observed in the  $a$  films, whereas low-valence species, such as tetravalent and pentavalent, were observed in addition to the hexavalent form in the  $spc$  films. When  $F_{\text{RPD}}(\text{O}_2)$  was reduced from 24 to 15%, the low-valence state did not appear in the  $a$  films; however, the defect states originating from the partially unsaturated indium cations and/or the large void defects originating from oxygen deficiencies, as mentioned earlier, appeared in the VB spectrum [Fig. 3(b-2)]. When the films were solid-phase crystallized, the defect-derived states disappeared, and defect states appeared in the band gap ( $E_b = 1.7\text{--}0.5$  eV), wherein the low-valence states were prominent in the W core level. The reduction of a certain amount of W and the oxidation of the matrix film can occur. Solid-phase crystallization of the thin films deposited under low- $F_{\text{RPD}}(\text{O}_2)$  conditions led to the substitution of  $\text{W}^{4+}$  with In, which acted as a monovalent donor.  $\text{W}^{4+}$  was assumed to be more dominant than  $\text{W}^{5+}$  because the behavior of the high-mobility film ( $96\text{ cm}^2\text{ V}^{-1}\text{ s}^{-1}$ ) could not be explained by the presence of doubly charged  $\text{W}_{\text{In}}^{2+}$  donors. The  $\text{H}_i^+$  and  $\text{H}_\text{O}^+$  donors also possibly existed in the film. Moreover, as  $F_{\text{RPD}}(\text{O}_2)$  increased, the  $\text{W}_{\text{In}}^+$  and  $\text{H}_\text{O}^+$  donors decreased in number, resulting in  $\text{W}_{\text{In}}^{3+}\text{O}_i^{2-}$  and  $\text{H}_i^+$  being the primary donors. With a further increase in  $F_{\text{RPD}}(\text{O}_2)$ ,  $\text{O}_i$  excessively increased and carrier compensation likely occurred. Therefore, the carrier density and mobility significantly decreased at the  $F_{\text{RPD}}(\text{O}_2)$  of 24% (Table I). The ionic radii of the six-coordinated  $\text{In}^{3+}$ ,  $\text{W}^{6+}$ ,  $\text{W}^{5+}$ , and  $\text{W}^{4+}$  are 80, 60, 62, and 66 pm, respectively.

Figure 5 summarizes the VB and VBM spectra of  $spc\text{-In}_2\text{O}_3\text{:H}$ ,  $\text{In}_2\text{O}_3\text{:W,H}$  ( $\text{WO}_3$ : 1 wt. %),  $\text{In}_2\text{O}_3\text{:Ce,H}$  ( $\text{CeO}_2$ : 1 wt. %),  $\text{In}_2\text{O}_3\text{:Ce,H}$  ( $\text{CeO}_2$ : 2 wt. %), and  $\text{In}_2\text{O}_3\text{:Sn,H}$  ( $\text{SnO}_2$ : 1 wt. %) with similar carrier densities; Fig. S2 in the

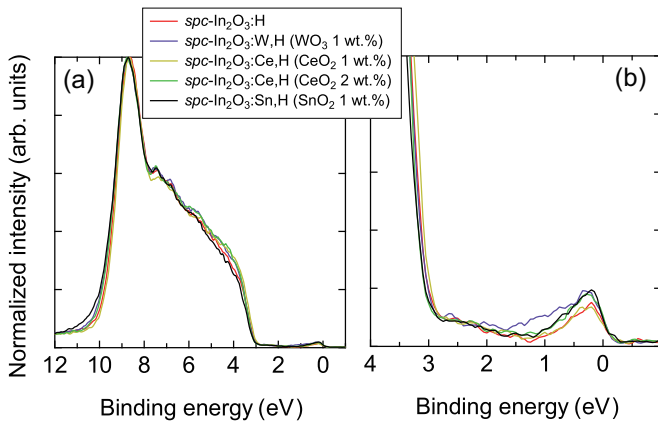


FIG. 5. Spectra near the (a) valence band and (b) VBM of *spc*-In<sub>2</sub>O<sub>3</sub>:H, In<sub>2</sub>O<sub>3</sub>:W,H, In<sub>2</sub>O<sub>3</sub>:Ce,H, and In<sub>2</sub>O<sub>3</sub>:Sn,H films with similar carrier densities.

Supplemental Material shows the In  $3d_{5/2}$  and O  $1s$  core levels [51]. The slight difference in the CBM emission intensity and the core level of the unscreened state can be explained by the difference in the carrier density. The essential differences depending on the type of metal impurity include the appearance of the Sn  $5s$ -derived state at the lower edge of the VB ( $E_b =$  approximately 10.5 eV) in Sn-doped films [58] and the appearance of states at the energy position,  $E_b = 1.7$ – $0.5$  eV, in W-doped films, which was also superimposed on the spectrum owing to the CBM emission. The Sn  $5s$ -derived states were more prominent in the ITO samples (3 and 5 wt. % SnO<sub>2</sub>), whereas the W-derived midgap states were more prominent in the *spc*-In<sub>2</sub>O<sub>3</sub>:W,H [ $F_{\text{RPD}}(\text{O}_2) = 15\%$ ] film that was prepared under O-poor conditions and postannealed [Fig. 3(b-2)]. The observed density of states reflects W  $5d$  orbitals because DFT calculations have suggested that they form a level below the CBM of In<sub>2</sub>O<sub>3</sub> [38]. However, there were no clear spectral differences between the In<sub>2</sub>O<sub>3</sub>:Ce,H thin films, including *spc*-

In<sub>2</sub>O<sub>3</sub>:Ce,H (3 wt. % CeO<sub>2</sub>) and In<sub>2</sub>O<sub>3</sub>:H. Therefore, the Ce  $4f$  orbitals were presumed to not form levels in the band gap, as confirmed by DFT calculations [37].

### C. Superior alternative dopants to Sn for In<sub>2</sub>O<sub>3</sub> to achieve high electron mobility

Figure 1(d-2) shows changes in the mobility of the *spc* films with varying  $F_{\text{MS}}(\text{O}_2)$ . The films doped with H only, H and Ce, H and Zr, and H, Ga, Ti, and Zr clearly exhibited higher mobility than that of H and Sn, which had similar carrier densities to that of low Sn concentrations. Figure 6 shows the variation in mobility of the films prepared by (a) MS and (b) RPD with different carrier densities. The data connected by straight lines represent the samples in which the  $F(\text{O}_2)$  during deposition was varied as in Fig. 1(d-2). A comparison of the electrical properties of the In<sub>2</sub>O<sub>3</sub>:H, In<sub>2</sub>O<sub>3</sub>:Ce,H, and In<sub>2</sub>O<sub>3</sub>:Sn,H films deposited by MS and RPD indicates the formation of films with similar properties under the optimized  $P_{\text{H}_2\text{O}}$  and  $F(\text{O}_2)$ . The *spc*-In<sub>2</sub>O<sub>3</sub>:H and In<sub>2</sub>O<sub>3</sub>:Ce,H (0.5–2 wt. % CeO<sub>2</sub>) films exhibited high mobility (150–160 cm<sup>2</sup> V<sup>-1</sup> s<sup>-1</sup>); the *spc*-In<sub>2</sub>O<sub>3</sub>:Zr,H (1 wt. % ZrO<sub>2</sub>), In<sub>2</sub>O<sub>3</sub>:Ga,Ti,Zr,H, and In<sub>2</sub>O<sub>3</sub>:W,H (1 wt. % WO<sub>3</sub>) films exhibited a relatively lower mobility ( $\sim 100$  cm<sup>2</sup> V<sup>-1</sup> s<sup>-1</sup>); and the *spc*-In<sub>2</sub>O<sub>3</sub>:Sn,H (1 wt. % SnO<sub>2</sub>) films exhibited a modest mobility of  $\sim 70$  cm<sup>2</sup> V<sup>-1</sup> s<sup>-1</sup>. The difference in values clearly reflects the influence of the metallic impurities.

To elucidate the higher mobility of these TM-doped films than those of the Sn-containing films, SE measurements were performed on these films at 65° and 70° angle of incidence. Figure 7(a) shows examples of the SE data measured at 70° angle of incidence for *spc*-In<sub>2</sub>O<sub>3</sub>:Ce,H and In<sub>2</sub>O<sub>3</sub>:Sn,H films. Thin films with similar electrical carrier density and different mobility were selected. The electrical properties (carrier density and mobility) determined using the Hall measurements for the *spc*-In<sub>2</sub>O<sub>3</sub>:Ce,H film with a thickness of 55 nm and *spc*-In<sub>2</sub>O<sub>3</sub>:Sn,H film with a thick-

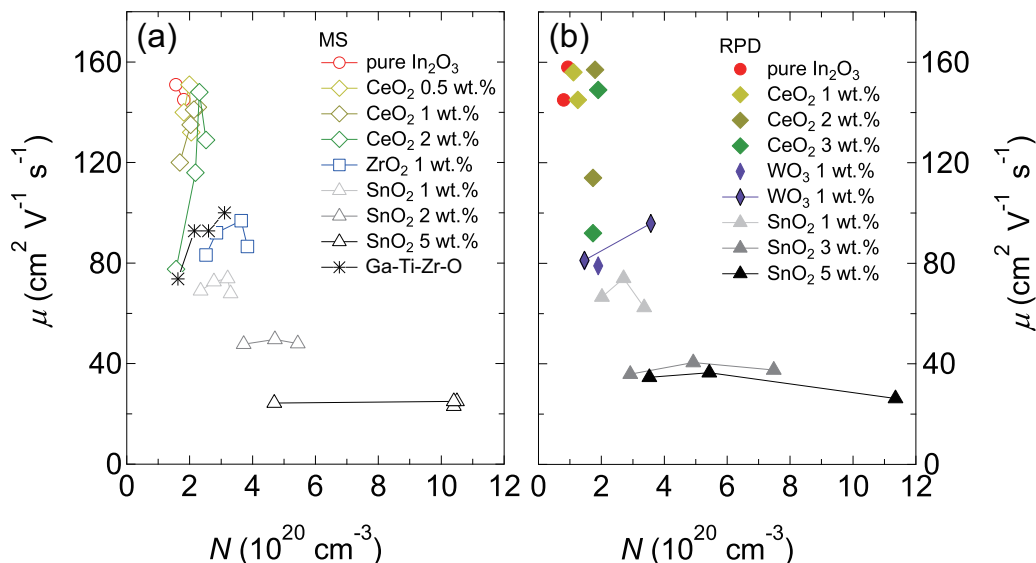


FIG. 6. Hall mobility ( $\mu$ ) as a function of Hall carrier density ( $N$ ) for *spc*-In<sub>2</sub>O<sub>3</sub>:Me,H films fabricated by (a) MS and (b) RPD using different ceramic targets and tablets, respectively.

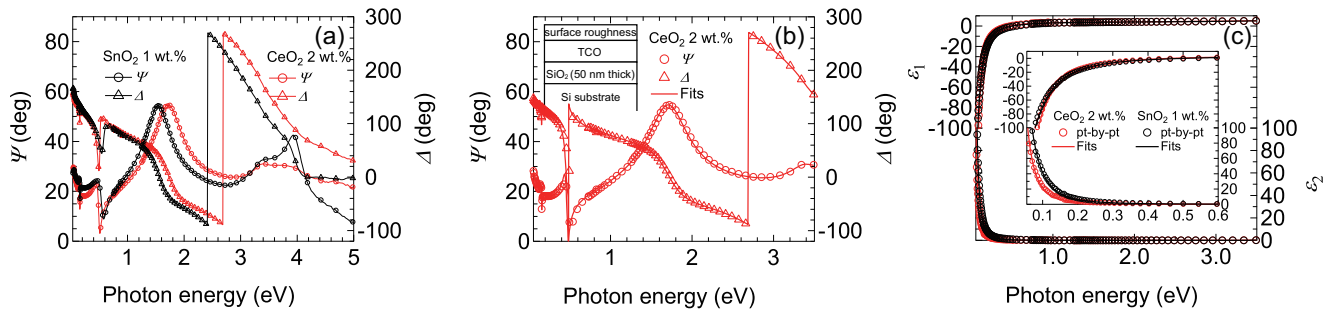


FIG. 7. (a) SE spectra obtained from the  $\text{spc-In}_2\text{O}_3\text{:Ce,H}$  (red) and  $\text{spc-In}_2\text{O}_3\text{:Sn,H}$  (black) films on  $\text{SiO}_2/\text{Si}$  substrates. (b) SE spectra and the result of the SE fitting analysis for the  $\text{spc-In}_2\text{O}_3\text{:Ce,H}$  sample. Optical model for a TCO layer formed on a  $\text{SiO}_2/\text{Si}$  substrate is also shown in the inset. (c) Extracted point-by-point fitted dielectric functions (open circle) and calculation result obtained from the parametrization assuming the TL and Drude models (solid line) for  $\text{spc-In}_2\text{O}_3\text{:Ce,H}$  and  $\text{spc-In}_2\text{O}_3\text{:Sn,H}$  films with similar electrical carrier density and different mobility. The inset shows the enlarged dielectric function in the infrared region. The open circles and triangles are drawn every ten data values for clarity.

ness of 70 nm were  $1.8 \times 10^{20}$  and  $2.0 \times 10^{20} \text{ cm}^{-3}$ , and 160 and  $67 \text{ cm}^2 \text{ V}^{-1} \text{ s}^{-1}$ , respectively. The difference in the measured SE spectra at infrared wavelength is mainly owing to the different in free-carrier absorption, which originates from the large difference in optical mobility. SE analyses of the thin films were performed using an optical model consisting of air/surface roughness layer/TCO/ $\text{SiO}_2$ /crystalline Si. Figure 7(b) shows the fitting results for the  $\text{spc-In}_2\text{O}_3\text{:Ce,H}$  film only, for clarity. The corresponding extracted point-by-point fitted dielectric functions and calculation result obtained from the parametrization assuming the TL and Drude models for the two films are shown in Fig. 7(c). The sum of the contributions almost completely described the point-by-point fitted results in the photon energy range from 0.055 to 3.5 eV. This range was used to avoid complex structure seen in the dielectric function at higher energies ( $E > 3.5 \text{ eV}$ ) and phonon absorption owing to  $\text{In}_2\text{O}_3$  ( $E < 0.055 \text{ eV}$ ). The two films exhibit similar plasma energies, but different Drude broadening parameters. This result indicates that the two thin films have very different optical mobility while having similar optical carrier densities. The effective mass and relaxation time of optical electrons for all the films were evaluated by SE. Optical mobility can be calculated using these values, and can be compared with the electrical mobility determined using the Hall measurements. The optical and electrical mobilities were comparable for all but one of the samples evaluated in this study [Fig. 8(a)]. This can be explained by the adequate passivation of the grain boundaries by chemisorbed H and OH with negligible potential barriers at the grain boundaries that interfere with electron transport [20,61]. The lower electrical mobility of the  $\text{In}_2\text{O}_3\text{:Ce,H}$  (2 wt. %  $\text{CeO}_2$ ) film fabricated at a high  $F_{\text{MS}}(\text{O}_2)$  compared to its optical mobility was because of the height of the barrier, which could not be neglected [20]. Moreover, the optical carrier density calculated from the effective mass and the Drude oscillator amplitude and the electrical carrier density are almost identical for all investigated samples [Fig. 8(b)].

Figure 9 shows plots of the optical mobility, effective mass, and relaxation time as a function of carrier density, in which the mobility decreases, effective mass increases, and relaxation time decreases with increasing

carrier densities; these trends can be explained by the non-parabolic nature of the conduction band [62,63] and ionization impurity scattering [41,64]. In the carrier density range of  $1\text{--}4 \times 10^{20} \text{ cm}^{-3}$ , a large variation in mobility was clearly observed, even at a fixed carrier density, depending on the added impurities and  $F(\text{O}_2)$ . Moreover, no effective differences were observed in the effective masses of electrons between low Sn-concentration  $\text{In}_2\text{O}_3$  and those with impurities other than Sn [Fig. 9(b)]. However, considerable differences were observed in the relaxation time of these films [Fig. 9(c)]. These results clearly demonstrate that the high mobility of the films can be attributed to the long relaxation time rather than the small effective mass. It is worth noting that the differences in mobility can be ascribed to the relaxation time even for the films with optimized  $F(\text{O}_2)$ . The films with a high carrier density were limited to the high Sn-concentration ITO, which had a large effective mass. More importantly, the carrier-compensated ITO films with high Sn concentration obtained by depositing the films under oxygen-rich conditions had a smaller effective mass than that of the films without carrier compensation, and the values were comparable to those of the TM-doped films with similar carrier densities. Therefore, the values of effective mass in this range of carrier densities were largely dependent on the carrier density, and were less sensitive to the

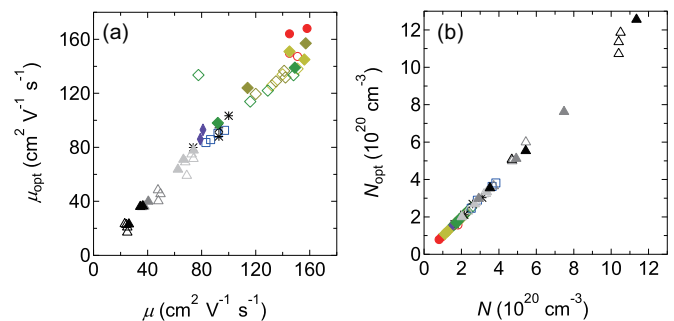


FIG. 8. (a) Optical mobility ( $\mu_{\text{opt}}$ ) as a function of Hall mobility ( $\mu$ ) and (b) optical carrier density ( $N_{\text{opt}}$ ) as a function of Hall carrier density ( $N$ ) for the  $\text{spc}$  films deposited by MS and RPD. The plot labels are identical to those shown in Fig. 6.

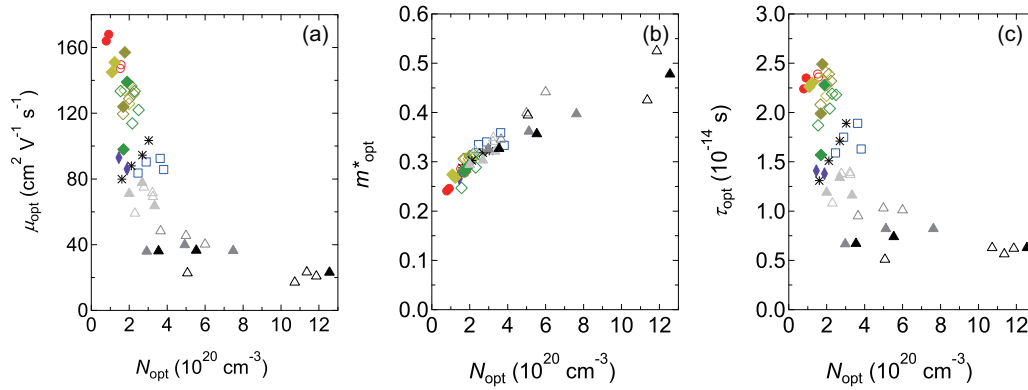


FIG. 9. (a) Optical mobility ( $\mu_{\text{opt}}$ ), (b) optical effective mass ( $m_{\text{opt}}^*/m_0$ ), and (c) carrier relaxation time ( $\tau_{\text{opt}}$ ) of the *spc* films deposited by MS and RPD as a function of optical carrier density ( $N_{\text{opt}}$ ). The plot labels are identical to those shown in Fig. 6.

metal impurities and their concentration. These results clearly show that the dispersion of the conduction band near  $E_f$  was almost independent of the type of metallic impurity (Sn, Ce, Zr, and W) at the investigated impurity and carrier concentrations. For high-concentration doping of Ce, W, or Zr, the dispersion of the conduction band has been computationally shown to exhibit large differences compared to that in ITO. However, in the  $\text{In}_2\text{O}_3:\text{TM,H}$  films fabricated by our MS and RPD methods, increasing the amount of TMs led to carrier compensation, which resulted in the high carrier density being restricted to  $4 \times 10^{20} \text{ cm}^{-3}$ . The differences in effective mass with respect to the TM elements and their concentrations at high carrier densities might be experimentally determined in the future. Only a limited number of reports exist on TM-doped thin films with high carrier densities [35,36].

The relaxation time is dominated by phonon and impurity scattering. Indeed, the temperature dependence of the Hall measurements for the *spc*- $\text{In}_2\text{O}_3:\text{TM,H}$  films revealed that phonon scattering affected the room-temperature mobility, as shown in Fig. 2(b). Because the crystal structure and lattice parameter of the *spc* films do not show significant differences with respect to the metal impurity [4], the phonon-dominated relaxation time of the thin films is presumably unaffected by the type of metal impurity. It is more natural to assume changes in the magnitude of the impurity scattering. Typically, the degree of ionized impurity scattering depends on the charge states of the impurities and a dielectric constant of the  $\text{In}_2\text{O}_3$  matrix. The photoelectron spectroscopy measurements indicate that the valence of each metal impurity was a mixture of trivalent and tetravalent for Ce, tetravalent for Zr, hexavalent and lower valences for W, and tetravalent for Sn. Therefore, Ce, Zr, and Sn can function as monovalent donors for  $\text{Me}_{\text{In}}^+$ , whereas W can act as a monovalent donor for  $\text{W}_{\text{In}}^+$  and  $\text{W}_{\text{In}}^{3+}\text{O}_i^{2-}$  and as a double donor for  $\text{W}_{\text{In}}^{2+}$ , depending on the In/O ratio. By contrast, the dielectric constant of the matrix was not considered to change owing to the impurities because of the extremely low concentration of the metal impurities ( $\sim 1$  at. %). Evidently, the high-frequency dielectric constant calculated by SE did not depend on the type of metal impurity (Fig. S3 in the Supplemental Material [51]). It is worth noting that the Lyddane-Sachs-Teller relation permits calculation of the static dielectric constant from the high-

frequency dielectric constant [63]. Therefore, all investigated films were expected to show similar relaxation times, except the W-doped films, based on the Brooks-Herring-Dingle formula, which has been successfully used to analyze the mobility dominated by ionized impurity scattering of ITO films [65]. However, the experimentally obtained relaxation times were remarkably different, with larger values determined for Ce, Zr, W, and Sn, in that order [Fig. 9(c)].

DFT calculations have shown that, unlike Sn 5s orbitals, TM *d* orbitals do not strongly interact with the In 5s orbitals that dominate the conduction band of  $\text{In}_2\text{O}_3$ , forming levels at energies well above the CBM or  $E_f$ , depending on the element [34–38]. Weak interactions are believed to occur with free electrons around the dopant in this context, which is a factor responsible for the high mobility of Mo 4*d* in  $\text{In}_2\text{O}_3$  [35,36]. Theoretical calculations have shown that the Ce 4*f* [37] and Zr 4*d* orbitals [38] form energy levels at energy positions considerably higher than the CBM, and the W 5*d* orbitals [38] form energy levels near the CBM. The photoemission spectra near the VBM shown in Sec. III B are consistent with the DFT calculation results. Therefore, if a similar phenomenon can be realized in Zr/Ce and H co-doped  $\text{In}_2\text{O}_3$ , they can exhibit a higher mobility than that of ITO.

Additionally, the number of O-derived defects ( $V_{\text{O}}$  and  $\text{O}_i$ ) in the films prepared at the optimal  $F(\text{O}_2)$  should change based on the added metal impurity. The standard formation enthalpies per mole of metal of  $\text{CeO}_2$ , and  $\text{ZrO}_2$  [46], which were mentioned earlier, and that of  $\text{WO}_3$  ( $-842.9 \text{ kJ mol}^{-1}$ ) are lower than those of  $\text{SnO}_2$  and  $\text{In}_2\text{O}_3$ . Therefore, owing to the similar chemical potentials of In, O, and electrons, the addition of Ce, Zr, and W is expected to increase the formation energy of  $V_{\text{O}}$  defects and decrease their concentration compared to those achieved by the addition of Sn [37,43,66]. If the concentration of  $\text{O}_i$ , which is an acceptor-type defect, is sufficiently low compared to that of donor-type defects in the films prepared at each optimal  $F(\text{O}_2)$ , and the  $V_{\text{O}}$  concentration of  $\text{In}_2\text{O}_3$  doped with Ce, Zr, and W is significantly lower than that of Sn-doped  $\text{In}_2\text{O}_3$ , a higher mobility than that of Sn-doped  $\text{In}_2\text{O}_3$  can be achieved.

Finally, the *spc*- $\text{In}_2\text{O}_3:\text{Me,H}$  films evaluated in this study exhibit the intrinsic performance of  $\text{In}_2\text{O}_3:\text{Me,H}$  materials despite their polycrystalline structure, because the grain struc-

ture is sufficiently larger than the mean-free path of free electrons, the grain boundaries are passivated by H, and the potential barrier to electron transport is negligible. In these films, impurities such as Me and H are solidly dissolved as metastable supersaturated solid solutions under the prescribed postannealing conditions. Conversely, it should be noted that postannealing conditions such as heating and cooling rates and atmosphere can affect structural defects such as point defects and native defects [67] and thereby electrical performance [14,20].

#### IV. CONCLUSIONS

In this study,  $\text{In}_2\text{O}_3:\text{H}$  and  $\text{In}_2\text{O}_3:\text{TM,H}$  were experimentally demonstrated to exhibit significantly higher mobility than that of  $\text{In}_2\text{O}_3:\text{Sn,H}$  at similar carrier densities ( $1\text{--}4 \times 10^{20} \text{ cm}^{-3}$ ). The *spc*- $\text{In}_2\text{O}_3:\text{H}$  and  $\text{In}_2\text{O}_3:\text{Ce,H}$  ( $\text{CeO}_2$ : 0.5–2 wt. %) films exhibited high mobility ( $150\text{--}160 \text{ cm}^2 \text{ V}^{-1} \text{ s}^{-1}$ ), *spc*- $\text{In}_2\text{O}_3:\text{Zr,H}$  ( $\text{ZrO}_2$ : 1 wt. %),  $\text{In}_2\text{O}_3 : \text{Ga, Ti, Zr, H}$ , and  $\text{In}_2\text{O}_3:\text{W,H}$  ( $\text{WO}_3$ : 1 wt. %) showed a relatively lower mobility ( $\sim 100 \text{ cm}^2 \text{ V}^{-1} \text{ s}^{-1}$ ), and *spc*- $\text{In}_2\text{O}_3:\text{Sn,H}$  ( $\text{SnO}_2$ : 1 wt. %) exhibited modest mobility ( $\sim 70 \text{ cm}^2 \text{ V}^{-1} \text{ s}^{-1}$ ). Photoelectron spectroscopy measurements of these films indicate that the electronic state of the *spc* films, including the valence of TM impurities, changed when the In/O ratio of the amorphous films was varied. Therefore, the compositions of In, O, TM, and H in the amorphous films were crucial to the effective activation of  $\text{TM}_{\text{In}}^+$ ,  $\text{H}_{\text{O}}^+$ , and  $\text{H}_{\text{i}}^+$  donors after crystallization. Furthermore, the photoemission spectra near the VBM revealed that states at the energy position,  $E_{\text{b}} = 1.7\text{--}0.5 \text{ eV}$ , appeared in the W-doped *spc* films whereas no new states in the band gap appeared in the Ce-doped *spc* films. The high electron mobility in the  $\text{In}_2\text{O}_3:\text{TM,H}$  films was investigated by evaluating the effective mass and relaxation

time of electrons by spectroscopic ellipsometry. The results show that the high mobility could be ascribed to the long relaxation time rather than the small effective mass. This indicates that the dispersion of conduction bands near the Fermi energy was almost independent of the type of metallic impurity (Sn, Ce, Zr, and W) at the investigated impurity concentrations. The TM doping-induced increase in relaxation time can be explained as follows: (1) The Zr *4d*, W *5d*, and Ce *4f* orbitals hardly interact with the In *5s* orbitals, which dominate the conduction band of  $\text{In}_2\text{O}_3$ , and Zr *4d* and Ce *4f* form levels at energies sufficiently higher than the CBM or  $E_{\text{f}}$ , resulting in modest interactions with the free electrons around the dopant. (2) The standard formation enthalpies per mole of metal of  $\text{CeO}_2$ ,  $\text{ZrO}_2$ ,  $\text{WO}_3$  are lower than those of  $\text{SnO}_2$  and  $\text{In}_2\text{O}_3$ , and the oxygen vacancy concentration can be suppressed at the optimal oxygen flow rate, thus inhibiting the scattering of ionized impurities.

#### ACKNOWLEDGMENTS

This study was partially supported by the National Institute of Advanced Industrial Science and Technology (AIST) and a JSPS KAKENHI grant (Grant No. 20K05339). The synchrotron radiation experiments were performed using the BL46XU beamline at SPring-8 with the approval of the Japan Synchrotron Radiation Research Institute (JASRI; Proposal No. 2020A1876). The authors express their sincere gratitude to Dr. Satoshi Yasuno of JASRI for assistance with the HAXPES measurements. T.K. would like to thank Dr. Leonard Tutsch for assistance with the  $\text{In}_2\text{O}_3:\text{Ce,H}$  deposition by MS at AIST. T.K. also would like to thank Yuko Ueno and Hirofumi Higuchi for assistance with the  $\text{In}_2\text{O}_3:\text{Me,H}$  deposition by RPD and maintenance of the deposition equipment, respectively.

- 
- [1] T. J. Coutts, D. L. Young, and T. A. Gessert, in *Handbook of Transparent Conductors*, edited by D. Ginley, H. Hosono, and D. C. Paine (Springer, Boston, 2011).
- [2] A. E. Delahoy and S. Guo, in *Handbook of Photovoltaic Science and Engineering*, edited by A. Luque and S. Hegedus, 2nd ed. (Wiley, Chichester, 2011).
- [3] T. Koida, in *Spectroscopic Ellipsometry for Photovoltaics Volume 1: Fundamental Principles and Solar Cell Characterization*, edited by H. Fujiwara and R. W. Collins (Springer, Cham, 2018), Vol. 212.
- [4] T. Koida, Y. Ueno, and H. Shibata,  $\text{In}_2\text{O}_3$ -based transparent conducting oxide films with high electron mobility fabricated at low process temperatures, *Phys. Status Solidi* **215**, 1700506 (2018).
- [5] T. Koida, H. Fujiwara, and M. Kondo, Hydrogen-doped  $\text{In}_2\text{O}_3$  as high-mobility transparent conductive oxide, *Jpn. J. Appl. Phys., Part 2 Lett.* **46**, L685 (2007).
- [6] T. Koida, H. Fujiwara, and M. Kondo, Reduction of optical loss in hydrogenated amorphous silicon/crystalline silicon heterojunction solar cells by high-mobility hydrogen-doped  $\text{In}_2\text{O}_3$  transparent conductive oxide, *Appl. Phys. Express* **1**, 041501 (2008).
- [7] K. Yamamoto, K. Yoshikawa, H. Uzu, and D. Adachi, High-efficiency heterojunction crystalline Si solar cells, *Jpn. J. Appl. Phys.* **57**, 08RB20 (2018).
- [8] L. Barraud, Z. C. Holman, N. Badel, P. Reiss, A. Descoedres, C. Battaglia, S. De Wolf, and C. Ballif, Hydrogen-doped indium oxide/indium tin oxide bilayers for high-efficiency silicon heterojunction solar cells, *Sol. Energy Mater. Sol. Cells* **115**, 151 (2013).
- [9] F. Meng, J. Shi, Z. Liu, Y. Cui, Z. Lu, and Z. Feng, High mobility transparent conductive W-doped  $\text{In}_2\text{O}_3$  thin films prepared at low substrate temperature and its application to solar cells, *Sol. Energy Mater. Sol. Cells* **122**, 70 (2014).
- [10] T. Watahiki, T. Furuhashi, T. Matsuura, T. Shinagawa, Y. Shirayanagi, T. Morioka, T. Hayashida, Y. Yuda, S. Kano, Y. Sakai, H. Tokioka, Y. Kusakabe, and H. Fuchigami, Rear-emitter Si heterojunction solar cells with over 23% efficiency, *Appl. Phys. Express* **8**, 021402 (2015).

- [11] E. Kobayashi, Y. Watabe, T. Yamamoto, and Y. Yamada, Cerium oxide and hydrogen co-doped indium oxide films for high-efficiency silicon heterojunction solar cells, *Sol. Energy Mater. Sol. Cells* **149**, 75 (2016).
- [12] M. Boccard, N. Rodkey, and Z. C. Holman, High-mobility hydrogenated indium oxide without introducing water during sputtering, *Energy Proc.* **92**, 297 (2016).
- [13] M. Morales-Masis, E. Rucavado, R. Monnard, L. Barraud, J. Holovsky, M. Despeisse, M. Boccard, and C. Ballif, Highly conductive and broadband transparent Zr-doped  $\text{In}_2\text{O}_3$  as front electrode for solar cells, *IEEE J. Photovoltaics* **8**, 1202 (2018).
- [14] L. Tutsch, H. Sai, T. Matsui, M. Bivour, M. Hermle, and T. Koida, The sputter deposition of broadband transparent and highly conductive cerium and hydrogen co-doped indium oxide and its transfer to silicon heterojunction solar cells, *Prog. Photovoltaics Res. Appl.* **29**, 835 (2021).
- [15] T. Koida, H. Sai, and M. Kondo,  $\text{In}_2\text{O}_3$ :H transparent conductive oxide films with high mobility and near infrared transparency for optoelectronic applications, *Surf. Eng.* **28**, 102 (2012).
- [16] G. C. E. Jost, A. N. Hamri, F. Köhler, and J. Hüpkes, Reliability aspects of hydrogen-doped indium oxide, *Phys. Status Solidi Appl. Mater. Sci.* **213**, 1751 (2016).
- [17] E. Kobayash, N. Nakamura, and Y. Watabe, in *27th European Photovoltaic Solar Energy Conference and Exhibition*, edited by S. Nowak, A. Jager-Waldau, and P. Helm (WIP, Frankfurt, Germany, 2012), pp. 1619–1623.
- [18] E. Kobayashi, N. Nakamura, K. Hashimoto, and Y. Watabe, in *28th European Photovoltaics Solar Energy Conference and Exhibition*, edited by A. Mine, A. Jager-Waldau, and P. Helm (WIP, Paris, France, 2013), pp. 691–694.
- [19] A. Cruz, D. Erfurt, R. Köhler, M. Dimer, E. Schneiderlöchner, and B. Stannowski, in *Photovoltaics Int.* (Sol. Media Ltd., London, 2020), Vol. 44, pp. 86–96.
- [20] T. Koida and Y. Ueno, Thermal and damp heat stability of high-mobility  $\text{In}_2\text{O}_3$ -based transparent conducting films fabricated at low process temperatures, *Phys. Status Solidi Appl. Mater. Sci.* **218**, 2000487 (2021).
- [21] C. Battaglia, J. Escarre, K. Soderstrom, L. Erni, L. Ding, G. Bugnon, A. Billet, M. Boccard, L. Barraud, S. De Wolf, F. Haug, M. Despeisse, and C. Ballif, Nanoimprint lithography for high-efficiency thin-film silicon solar cells, *Nano Lett.* **11**, 661 (2011).
- [22] H. Sai, T. Matsui, and K. Matsubara, Stabilized 14.0%-efficient triple-junction thin-film silicon solar cell, *Appl. Phys. Lett.* **109**, 183506 (2016).
- [23] T. Koida, J. Nishinaga, Y. Ueno, H. Higuchi, H. Takahashi, M. Iioka, Y. Kamikawa, H. Shibata, and S. Niki, Improved efficiency of  $\text{Cu}(\text{In,Ga})\text{Se}_2$  mini-module via high-mobility  $\text{In}_2\text{O}_3$ :W,H transparent conducting oxide layer, *Prog. Photovoltaics Res. Appl.* **27**, 491 (2019).
- [24] J. Keller, A. Aijaz, F. Gustavsson, T. Kubart, L. Stolt, M. Edoff, and T. Törndahl, Direct comparison of atomic layer deposition and sputtering of  $\text{In}_2\text{O}_3$ :H used as transparent conductive oxide layer in  $\text{CuIn}_{1-x}\text{Ga}_x\text{Se}_2$  thin film solar cells, *Sol. Energy Mater. Sol. Cells* **157**, 757 (2016).
- [25] E. Aydin, M. De Bastiani, X. Yang, M. Sajjad, F. Aljamaan, Y. Smirnov, M. N. Hedhili, W. Liu, T. G. Allen, L. Xu, E. Van Kerschaver, M. Morales-Masis, U. Schwingenschlögl, and S. De Wolf, Zr-doped indium oxide (IZRO) transparent electrodes for perovskite-based tandem solar cells, *Adv. Funct. Mater.* **29**, 1901741 (2019).
- [26] H. Li and W. Zhang, Perovskite tandem solar cells: From fundamentals to commercial deployment, *Chem. Rev.* **120**, 9835 (2020).
- [27] T. Maeda, K. Oishi, H. Ishii, W. H. Chang, T. Shimizu, A. Endoh, H. Fujishiro, and T. Koida, High and broadband sensitivity front-side illuminated InGaAs photo field-effect transistors (PhotoFETs) with SWIR transparent conductive oxide (TCO) gate, *Appl. Phys. Lett.* **119**, 192101 (2021).
- [28] C. G. Van de Walle, Hydrogen as a Cause of Doping in Zinc Oxide, *Phys. Rev. Lett.* **85**, 1012 (2000).
- [29] Ç. Kiliç and A. Zunger, N-type doping of oxides by hydrogen, *Appl. Phys. Lett.* **81**, 73 (2002).
- [30] C. G. Van de Walle, Universal alignment of hydrogen levels in semiconductors and insulators, *Nature (London)* **423**, 626 (2003).
- [31] S. Limpijumnong, P. Reunchan, A. Janotti, and C. G. Van de Walle, Hydrogen doping in indium oxide: An ab initio study, *Phys. Rev. B* **80**, 193202 (2009).
- [32] M. Wagner, P. Lackner, S. Seiler, A. Brunsch, R. Bliem, S. Gerhold, Z. Wang, J. Osiecki, K. Schulte, L. A. Boatner, M. Schmid, B. Meyer, and U. Diebold, Resolving the structure of a well-ordered hydroxyl overlayer on  $\text{In}_2\text{O}_3(111)$ : Nanomanipulation and theory, *ACS Nano* **11**, 11531 (2017).
- [33] A. Samanta, J. B. Varley, and V. Lordi, Analysis of defects in  $\text{In}_2\text{O}_3$ :H synthesized in presence of water vapor and hydrogen gas mixture, *J. Appl. Phys.* **129**, 045102 (2021).
- [34] J. E. Medvedeva, Magnetically Mediated Transparent Conductors:  $\text{In}_2\text{O}_3$  Doped with Mo, *Phys. Rev. Lett.* **97**, 086401 (2006).
- [35] D. S. Bhachu, D. O. Scanlon, G. Sankar, T. D. Veal, R. G. Egdell, G. Cibir, A. J. Dent, C. E. Knapp, C. J. Carmalt, and I. P. Parkin, Origin of high mobility in molybdenum-doped indium oxide, *Chem. Mater.* **27**, 2788 (2015).
- [36] J. E. N. Swallow, B. A. D. Williamson, S. Sathasivam, M. Birkett, T. J. Featherstone, P. A. E. Murgatroyd, H. J. Edwards, Z. W. Lebens-Higgins, D. A. Duncan, M. Farnworth, P. Warren, N. Peng, T. L. Lee, L. F. J. Piper, A. Regoutz, C. J. Carmalt, I. P. Parkin, V. R. Dhanak, D. O. Scanlon, and T. D. Veal, Resonant doping for high mobility transparent conductors: The case of Mo-doped  $\text{In}_2\text{O}_3$ , *Mater. Horiz.* **7**, 236 (2020).
- [37] E. L. Runnerstrom, A. Bergerud, A. Agrawal, R. W. Johns, C. J. Dahlman, A. Singh, S. M. Selbach, and D. J. Milliron, Defect engineering in plasmonic metal oxide nanocrystals, *Nano Lett.* **16**, 3390 (2016).
- [38] J. Xu, J. B. Liu, B. X. Liu, S. N. Li, S. H. Wei, and B. Huang, Design of N-type transparent conducting oxides: The case of transition metal doping in  $\text{In}_2\text{O}_3$ , *Adv. Electron. Mater.* **4**, 1700553 (2018).
- [39] M. Fukumoto, Y. Hirose, B. A. D. Williamson, S. Nakao, K. Kimura, K. Hayashi, Y. Sugisawa, D. Sekiba, D. O. Scanlon, and T. Hasegawa, Ligand field-induced exotic dopant for infrared transparent electrode: W in rutile  $\text{SnO}_2$ , *Adv. Funct. Mater.* **32**, 2110832 (2022).
- [40] Y. Yoshida, D. M. Wood, T. A. Gessert, and T. J. Coutts, High-mobility, sputtered films of indium oxide doped with molybdenum, *Appl. Phys. Lett.* **84**, 2097 (2004).
- [41] T. Koida, M. Kondo, K. Tsutsumi, A. Sakaguchi, M. Suzuki, and H. Fujiwara, Hydrogen-doped  $\text{In}_2\text{O}_3$  transparent conduct-

- ing oxide films prepared by solid-phase crystallization method, *J. Appl. Phys.* **107**, 033514 (2010).
- [42] K. O. Egbo, A. E. Adesina, C. V. Ezeh, C. P. Liu, and K. M. Yu, Effects of free carriers on the optical properties of high mobility transition metal doped  $\text{In}_2\text{O}_3$  transparent conductors, *Phys. Rev. Mater.* **5**, 094603 (2021).
- [43] T. Koida and M. Kondo, Improved near-infrared transparency in sputtered  $\text{In}_2\text{O}_3$ -based transparent conductive oxide thin films by Zr-doping, *J. Appl. Phys.* **101**, 063705 (2007).
- [44] K. Iwata, T. Sakemi, A. Yamada, P. Fons, K. Awai, T. Yamamoto, S. Shirakata, K. Matsubara, H. Tampo, K. Sakurai, S. Ishizuka, and S. Niki, Improvement of ZnO TCO film growth for photovoltaic devices by reactive plasma deposition (RPD), *Thin Solid Films* **480-481**, 199 (2005).
- [45] H. Kitami, M. Miyashita, T. Sakemi, Y. Aoki, and T. Kato, Quantitative analysis of ionization rates of depositing particles in reactive plasma deposition using mass-energy analyzer and Langmuir probe, *Jpn. J. Appl. Phys.* **54**, 01AB05 (2015).
- [46] W. M. Haynes, *CRC Handbook of Chemistry and Physics*, 95th ed. (CRD Press, Boca Raton, 2014).
- [47] K. Ellmer and R. Mientus, Carrier transport in polycrystalline transparent conductive oxides: A comparative study of zinc oxide and indium oxide, *Thin Solid Films* **516**, 4620 (2008).
- [48] T. Koida and M. Kondo, High electron mobility of indium oxide grown on yttria-stabilized zirconia, *J. Appl. Phys.* **99**, 123703 (2006).
- [49] I. Chatratin, F. P. Sabino, P. Reunchan, S. Limpijumngong, J. B. Varley, C. G. Van de Walle, and A. Janotti, Role of point defects in the electrical and optical properties of  $\text{In}_2\text{O}_3$ , *Phys. Rev. Mater.* **3**, 074604 (2019).
- [50] R. Muysinov, A. Steigert, M. Wollgarten, P. P. Michałowski, U. Bloeck, A. Pflug, D. Erfurt, R. Klenk, S. Körner, I. Lauermann, and B. Szyszka, Crystallisation phenomena of  $\text{In}_2\text{O}_3$ :H Films, *Materials (Basel)* **12**, 266 (2019).
- [51] See Supplemental Material at <http://link.aps.org/supplemental/10.1103/PhysRevMaterials.6.055401> for core-level spectra of In ( $\text{In}3d_{5/2}$ ) and O ( $\text{O}1s$ ) and high-frequency dielectric constants for thin films.
- [52] J. Rosen and O. Warschkow, Electronic structure of amorphous indium oxide transparent conductors, *Phys. Rev. B: Condens. Matter Mater. Phys.* **80**, 115215 (2009).
- [53] A. Aliano, A. Catellani, and G. Cicero, Characterization of amorphous  $\text{In}_2\text{O}_3$ : An *ab initio* molecular dynamics study, *Appl. Phys. Lett.* **99**, 211913 (2011).
- [54] A. Klein, Electronic properties of  $\text{In}_2\text{O}_3$  surfaces, *Appl. Phys. Lett.* **77**, 2009 (2000).
- [55] T. Kamiya, K. Nomura, and H. Hosono, Electronic structure of the amorphous oxide semiconductor  $a\text{-LnGaZnO}_{4-x}$ : Tauc-Lorentz optical model and origins of subgap states, *Phys. Status Solidi Appl. Mater. Sci.* **206**, 860 (2009).
- [56] B. Ryu, H. K. Noh, E. A. Choi, and K. J. Chang, O-vacancy as the origin of negative bias illumination stress instability in amorphous In-Ga-Zn-O thin film transistors, *Appl. Phys. Lett.* **97**, 022108 (2010).
- [57] Y. Gassenbauer, R. Schafraneck, A. Klein, S. Zafeiratos, M. Hävecker, A. Knop-Gericke, and R. Schlögl, Surface states, surface potentials, and segregation at surfaces of tin-doped  $\text{In}_2\text{O}_3$ , *Phys. Rev. B: Condens. Matter Mater. Phys.* **73**, 245312 (2006).
- [58] C. Körber, V. Krishnakumar, A. Klein, G. Panaccione, P. Torelli, A. Walsh, J. L. F. Da Silva, S. H. Wei, R. G. Egdell, and D. J. Payne, Electronic structure of  $\text{In}_2\text{O}_3$  and Sn-doped  $\text{In}_2\text{O}_3$  by hard x-ray photoemission spectroscopy, *Phys. Rev. B: Condens. Matter Mater. Phys.* **81**, 165207 (2010).
- [59] A. Allahgholi, J. I. Flege, S. Thieß, W. Drube, and J. Falta, Oxidation-state analysis of ceria by x-ray photoelectron spectroscopy, *ChemPhysChem* **16**, 1083 (2015).
- [60] R. D. Shannon, Revised effective ionic radii and systematic studies of interatomic distances in halides and chalcogenides, *Acta Crystallogr. Sect. A* **32**, 751 (1976).
- [61] H. F. Wardenga, M. V. Frischbier, M. Morales-Masis, and A. Klein, In situ Hall effect monitoring of vacuum annealing of  $\text{In}_2\text{O}_3$ :H thin films, *Materials (Basel)* **8**, 561 (2015).
- [62] M. Feneberg, J. Nixdorf, C. Lidig, R. Goldhahn, Z. Galazka, O. Bierwagen, and J. S. Speck, Many-electron effects on the dielectric function of cubic  $\text{In}_2\text{O}_3$ : Effective electron mass, band nonparabolicity, band gap renormalization, and Burstein-Moss shift, *Phys. Rev. B* **93**, 045203 (2016).
- [63] M. Stokey, R. Korlacki, S. Knight, A. Ruder, M. Hilfiker, Z. Galazka, K. Irmscher, Y. Zhang, H. Zhao, V. Darakchieva, and M. Schubert, Optical phonon modes, static and high-frequency dielectric constants, and effective electron mass parameter in cubic  $\text{In}_2\text{O}_3$ , *J. Appl. Phys.* **129**, 225102 (2021).
- [64] B. Macco, H. C. M. Knoop, and W. M. M. Kessels, Electron scattering and doping mechanisms in solid-phase-crystallized  $\text{In}_2\text{O}_3$ :H prepared by atomic layer deposition, *ACS Appl. Mater. Interfaces* **7**, 16723 (2015).
- [65] Y. Shigesato and D. C. Paine, Study of the effect of Sn doping on the electronic transport properties of thin film indium oxide, *Appl. Phys. Lett.* **62**, 1268 (1993).
- [66] A. Murat and J. E. Medvedeva, Composition-dependent oxygen vacancy formation in multicomponent wide-band-gap oxides, *Phys. Rev. B: Condens. Matter Mater. Phys.* **86**, 085123 (2012).
- [67] R. C. Hoffmann, M. Kaloumenos, S. Heinschke, E. Erdem, P. Jakes, R. A. Eichel, and J. J. Schneider, Molecular precursor derived and solution processed indium-zinc oxide as a semiconductor in a field-effect transistor device. Towards an improved understanding of semiconductor film composition, *J. Mater. Chem. C* **1**, 2577 (2013).